Nonlinearity modulation based multiple Fano resonance and multi-spectral switching in a nanoplasmonic waveguide-coupled cavity system

S. Paul, and M. Ray

Citation: Journal of Applied Physics **124**, 193104 (2018); doi: 10.1063/1.5052694
View online: https://doi.org/10.1063/1.5052694
View Table of Contents: http://aip.scitation.org/toc/jap/124/19
Published by the American Institute of Physics

Nonlinearity modulation based multiple Fano resonance and multi-spectral switching in a nanoplasmonic waveguide-coupled cavity system

S. Paul and M. Ray[a)]
Department of Applied Optics and Photonics, University of Calcutta, Technology Campus, JD-2, Sector-3, Salt Lake, Kolkata 700106, India

(Received 21 August 2018; accepted 31 October 2018; published online 20 November 2018)

Dual and multiple asymmetric Fano resonance are theoretically explored in a subwavelength plasmonic cavity-coupled waveguide system incorporated with a third order Kerr nonlinear medium. The degree of asymmetry and the number of multiple resonances are controlled by an external pump beam which modulates the Kerr permittivity thereby dictating the resonant behavior. Electromagnetically induced transparency in plasmonic systems, referred to as plasmon induced transparency, is a special case of Fano resonance and plays a key role for the occurrence of multiple Fano excitations. Plasmon induced transparency appears as induced reflectance dips when analyzed in reflection mode. Though geometrical dependency of dual and multiple Fano effect is demonstrated, the main interest and importance is focused on the generation and manipulation of multiple Fano resonances by intensity modulation of the pump beam and its application in multispectral switching and quality factor tuning at a fixed operating frequency. *Published by AIP Publishing.* https://doi.org/10.1063/1.5052694

I. INTRODUCTION

Plasmonics has paved the way for the localization and control of light below the diffraction limit owing to the generation of surface plasmon polaritons (SPPs) which are quasiparticles originating from photon coupled quantized free charge oscillations at metal-dielectric interfaces.[1,2] Deep nanoscale optical mode confinement by plasmonic waveguide (WG) structures comprising of subwavelength metal-dielectric-metal (MDM) waveguides (WGs) coupled to one or several resonant cavities leads to the realization of highly integrated photonic circuits.[3] Both theoretical and experimental investigations on MDM WG based structures are reported in abundance for various applications.[4–7] The electromagnetic response of MDM WGs is often characterized by a unique resonant effect termed as Fano resonance (FR), originating from the interference of a discrete localized state and a continuum of states. Discovered by Ugo Fano in 1961, Fano resonance (FR) is typically marked by a sharp asymmetric resonant profile unlike the symmetric Lorentzian line shape.[8–10] The broad continuum state (with a strong coupling effect) exhibits a slow variation of energy compared to the quick transition of a narrow discrete state (with a weak coupling effect), and this rapid variation contributes to the asymmetric excitation. At resonance, the discrete (DM) and continuum mode (CM) bears different frequencies. However, if the frequencies of the two interfering states become identical, FR appears as electromagnetically induced transparency (EIT), usually observed in atomic systems.[11–13] Plasmonic analog of EIT, referred to as plasmon induced transparency (PIT), is thus a special case of FR and is characterized by a narrow transmission peak in the center of a broader transmission dip.[14,15] In the case of PIT, the asymmetry of the resonant line shape almost disappears because of the matched frequencies of the interfering modes. The sharp nature of PIT and FR are copiously explored and applied profusely in different plasmonic systems.[16–19] Apart from metal plasmonics, the appealing feature of PIT is also observed in graphene-based plasmonic systems such as in graphene nanoribbons.[20] Graphene structure composed of sinusoidally curved and planar layers also exhibits dynamically tunable PIT.[21,22] Double and multiple Fano and PIT resonant effects are reported in various metallic nanoplasmonic structures[23,24] and in different subwavelength MDM WG systems.[25–27] PIT observed in reflection mode would appear as a sharp narrow reflectance dip in the center of a broader reflectance peak and hence the term induced reflectance dip (IRD) has been coined by us to convey PIT in reflection mode.

Dramatic enhancement of intensity at the interfaces due to SPP localization boosts the occurrence of a nonlinear phenomenon at much lower threshold intensities compared to that required for the optical counterparts.[28,29] The ability to control the system response by modulating the nonlinearity through an additional pump beam has been explored by several researchers to study optical switching in MDM WG systems.[30–33] Optical switches with quick switching time and high contrast ratio can be achieved with Fano resonance because of quick transition from high to low transmittance (or reflectance) or vice versa.[34,35] Moreover, multiple Fano resonance (MFR) can be exploited to achieve switching at multiple wavelengths simultaneously.

In the present paper, we have considered a nonlinear dual cavity coupled subwavelength waveguide system, exhibiting dual and multiple Fano resonance. Tailoring of dual Fano resonance (DFR) spectra via intensity variation and structural alteration is investigated in detail. Intensity modulation leading to the occurrence of IRD, followed by the evolution of dual induced reflection dips (DIRD) and finally the achievement of multiple IRD (MIRD) leading to MFR is

[a)]Author to whom correspondence should be addressed: mraphy@caluniv.com

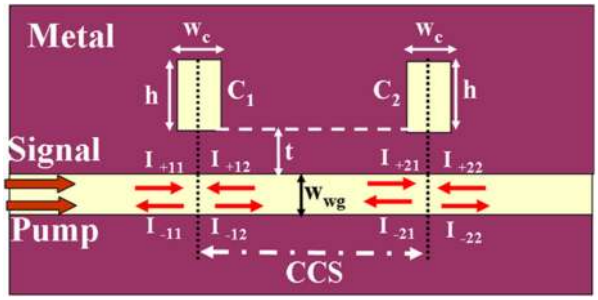

FIG. 1. Cross-sectional schematic representation of the MDM waveguide side coupled to dual nanocavities.

exhibited. Single and multispectral switching (MS) are demonstrated. DIRD is employed to obtain four wavelength switching, and simultaneous switching up to seven wavelengths is implemented by the application of MFR. Performance of the switch for all switching wavelengths (SWs) is determined. Regulating resonance frequencies of MFR by the external control beam is also applied to achieve spectral width tuning or consequently quality factor tuning at fixed wavelengths providing a platform to achieve a tunable filter with varying bandwidth at a fixed operating frequency without the need for any structural variation.

II. STRUCTURE DESCRIPTION AND THEORETICAL MODELING

The nanoplasmonic structure under consideration is depicted in Fig. 1. It comprises a MDM waveguide of width w_{wg} side coupled to two identical nanocavities C_1 and C_2, each of height h and width w_c. Subwavelength widths (w_{wg}, $w_c \ll \lambda$) ensure fundamental antisymmetric single mode propagation of the transverse magnetic surface plasmon polariton (TM-SPP) wave in the waveguide (WG) when suitably illuminated by an incident beam (Signal) of wavelength λ. The TM-SPP mode gets coupled into the cavities due to the tunneling effect through the coupling distance t. Cavity-cavity separation (CCS) is such that only indirect coupling between the cavities is supported. The WG and the cavities are embedded in a silver (Ag) metal substrate whose frequency dependent optical permittivity is determined using the Drude dispersion model[36] given by

$$\varepsilon_m = 1 - \frac{\lambda^2 \lambda_c}{\lambda_p^2(\lambda_c + i\lambda)}, \tag{1}$$

where λ_p and λ_c denote the plasma and collision wavelength, respectively. For nonlinear operation, the WG and the cavities are filled with a third order Kerr nonlinear medium having susceptibility $\chi^{(3)}$ and its nonlinear permittivity ε_{nl} can be altered by modulating the intensity I of the pump beam according to the equation $\varepsilon_{nl} = \varepsilon_l + \chi^{(3)}I$, ε_l being the linear permittivity term, independent of applied intensity.

The propagating waves within the waveguide strongly depend on the cavity-cavity phase or CCP (φ) of the SPP wave, satisfying the relations: $I_{+12} = I_{-21}\exp(i\varphi)$ and $I_{+21} = I_{-12}\exp(i\varphi)$, where φ is evaluated as $\varphi = 2\pi \mathrm{Re}(n_{eff})CCS/\lambda$ and n_{eff} represents the effective refractive index which can be determined using the coupled SPP approximation[37] given by

$$n_{eff} = \left[\varepsilon_{nl}\left(1 + \frac{\lambda}{\pi w\sqrt{-\varepsilon_m}}\sqrt{1 + \frac{\varepsilon_{nl}}{-\varepsilon_m}}\right)\right]^{1/2}. \tag{2}$$

Here $w = w_c = w_{wg}$. Spectral response of the system is analyzed using a temporal coupled mode theory[38,39] and considering the launching of light from the left port ($I_{+22} = 0$), the reflectance can be calculated as $R = |r|^2 = |I_{-11}/I_{+11}|^2$ where the complex reflection coefficient r is given by $r = e^{i\varphi}(r_1 - r_2)$ and the reflection coefficients r_1 and r_2 of continuum and discrete mode are expressed as

$$r_1 = \frac{\kappa_1(1 - \cos\varphi)}{i(\Delta\omega - \kappa_1 \sin\varphi) + \kappa_0 + \kappa_1(1 - \cos\varphi)}, \tag{3}$$

$$r_2 = \frac{\kappa_1(1 + \cos\varphi)}{i(\Delta\omega + \kappa_1 \sin\varphi) + \kappa_0 + \kappa_1(1 + \cos\varphi)}. \tag{4}$$

In the above equations, $\Delta\omega = \omega_0 - \omega$, where ω_0 denotes the resonance frequency of the cavities. κ_0 and κ_1 are the field decay rates due to internal loss in cavities and due to power escape from the cavities through the WG, respectively. $\omega_0 \pm \kappa_1 \sin\varphi$ and $\kappa_1(1 \pm \cos\varphi)$ are the modified frequencies and decay rates, respectively, of the two resonance modes r_1 and r_2. As Fano resonance occurs due to interference of the two modes, the total reflectance can also be represented in terms of coherent interference of r_1 and r_2 as $R = |r_1|^2 + |r_2|^2 + 2|r_1||r_2|\cos\theta$, where θ is the phase difference between the two modes.

The nanoplasmonic cavity coupled waveguide structure has been designed by considering the Kerr medium to be a nonlinear organic polymer with $\kappa^{(3)} = 1.95 \times 10^{-3}$ $\mu m^2/V^2$ and $\varepsilon_l = 2.3$.[40] Geometrical parameters chosen are $w_{wg} = w_c = 50$ nm, h = 250 nm, and t = 5 nm. Resonance

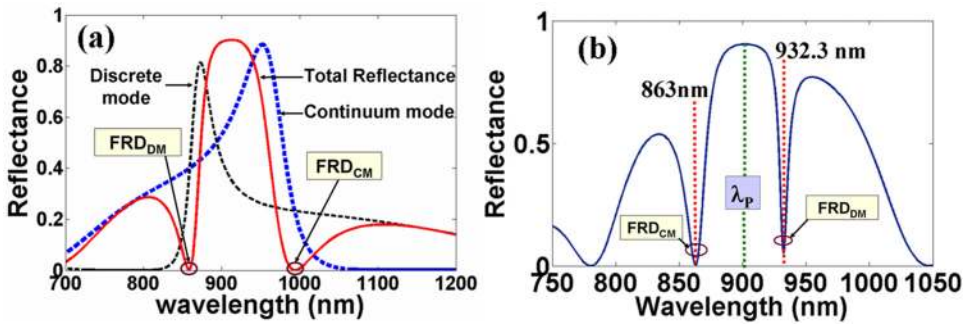

FIG. 2. (a) Spectral response of the considered system for the continuum mode, discrete mode, and total reflectance exhibiting dual Fano resonance. CCS = 400 nm and $I = 1000\ V^2/\mu m^2$. (b) Existence of DFR for CCS = 290 nm and $I = 20\,250\ V^2/\mu m^2$.

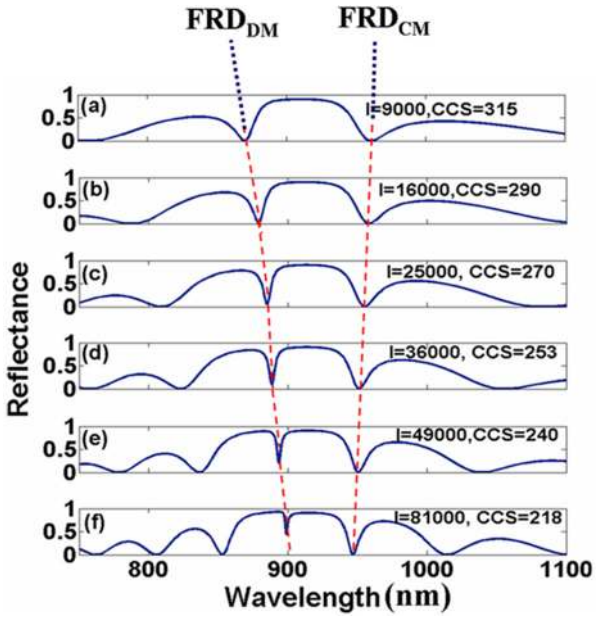

FIG. 3. Tailoring dual Fano resonance (DFR) by simultaneous variation of applied intensity (I in $V^2/\mu m^2$) and cavity-cavity separation (CCS in nm) as mentioned in the plots.

frequency $\omega_0 = 2.076 \times 10^{15}$ rad/s and value of coupling rates are $\kappa_0 = 5.2 \times 10^{12}$ rad/s and $\kappa_1 = 1 \times 10^{14}$ rad/s.

III. ANALYSIS OF DUAL AND MULTIPLE FANO RESONANCE

A. Dual Fano resonance in the nonlinear cavity coupled plasmonic waveguide

Reflectance spectra of the nonlinear plasmonic structure for the continuum mode r_1, discrete mode r_2, and total

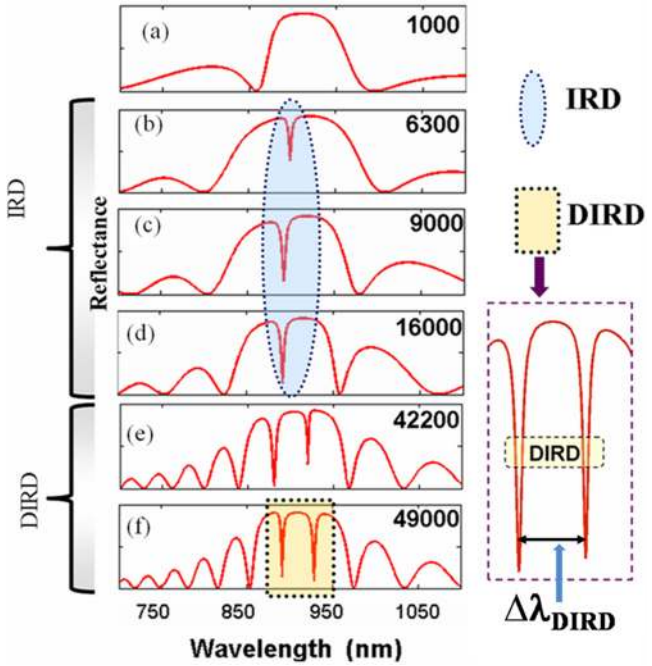

FIG. 4. Spectral response of the nanoplasmonic system with varying applied intensity for CCS = 400 nm. Value of the applied intensity having unit $V^2/\mu m^2$ is mentioned in the top right corner of the individual plots. Intensity is increased from (a) to (f).

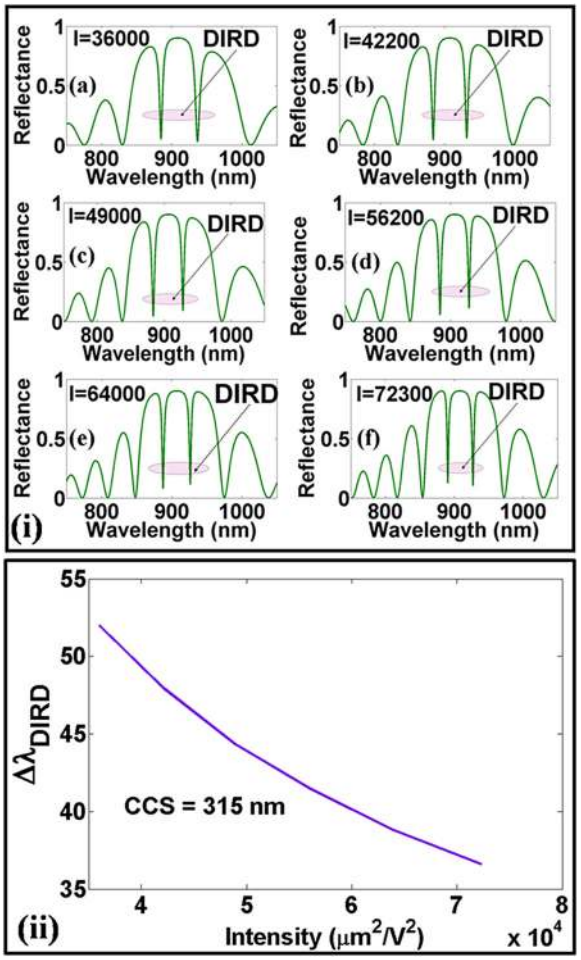

FIG. 5. (i) DFR exhibited as DIRD for different applied intensities (I) in ascending order from (a) to (f) for CCS = 315 nm. Unit of I mentioned in the plots is $V^2/\mu m^2$. (ii) $\Delta\lambda_{DIRD}$ is plotted for varying intensity.

reflectance R are depicted in Fig. 2(a). The discrete mode reflectance manifests narrow spectral width with full width half maxima (FWHM) of 31.9 nm compared to the broader width of the continuum mode with FWHM of 85.2 nm. The total reflectance which arises from the interference of the continuum and discrete mode exhibits two asymmetric Fano resonant dips (FRDs), one at 858.2 nm which lies near the peak of the discrete mode and is termed as FRD_{DM}

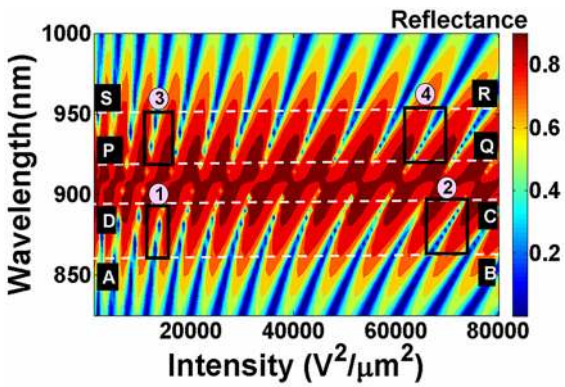

FIG. 6. Reflectance contour for wavelength and intensity variation for CCS = 400 nm.

indicating FRD due to discrete mode (DM), and the other one represented as FRD_{CM} depicting FRD due to continuum mode (CM), located at 994.3 nm near the peak of the continuum mode. The spectral widths corresponding to FRD_{DM} are observed to be narrower than FRD_{CM}, as expected. The occurrence of DFR can be attributed to the incorporation of nonlinearity activated by an external pump beam unlike that of a single Fano dip which originates in case of a simple dielectric medium used in the waveguide and the cavities of the plasmonic nanostructure considered in Ref. 9.

To ensure the occurrence of DFR for CCS and intensity value other than that considered in Fig. 2(a), a simulated result manifesting DFR for CCS = 290 nm and I = 20 250 $V^2/\mu m^2$ is plotted in Fig. 2(b). The figure depicts two asymmetric Fano reflection dips at 863 nm and 932.3 nm owing to CM and DM, respectively. However, both the Fano spectra are seen to be much narrower compared to the former result, particularly the sharpness corresponding to FRD_{DM} being remarkably enhanced. This is accounted to have occurred due to stronger field coupling resulting from the enhancement of intensity or reduced CCS or both. Also, the spectral distance between the two FR dips (let it be designated by $\Delta\lambda_{FR}$) is lower in the case of Fig. 2(b) ($\Delta\lambda_{FR} \approx 69$ nm) compared to $\Delta\lambda_{FR} \approx 136$ nm in the case of Fig. 2(a). Apart from tailoring of $\Delta\lambda_{FR}$ with a parametric change, another noticeable observation is that the occurrence of FRD_{CM} and FRD_{DM} is blue and red shifted, respectively, in Fig. 2(b) with respect to the central peak wavelength (λ_P) compared to the red and blue shift of FRD_{CM} and FRD_{DM} in Fig. 2(a). This spectral flipping of FRD_{CM} and FRD_{DM} about λ_P is accounted to the change of cavity-cavity phase (φ) which strongly determines the nature of the asymmetric profile by significantly modulating the resonant excitation wavelengths.[9]

By observing and comparing both the plots of Fig. 2, one can infer that the resonance wavelength and $\Delta\lambda_{FR}$ can be controlled by altering the applied intensity or structural parameter (CCS) or both. So to investigate the pattern of this modulation, Figs. 3(a)–3(f) are plotted with a simultaneous reduction of CCS and an increment of intensity. It is observed from Figs. 3(a)–3(f) that as the intensity increases with a simultaneous reduction in CCS, FRD_{DM} shows red shift and FRD_{CM} depicts blue shift thereby gradually reducing the FWHM of the central reflectance peak or, in other words, reducing $\Delta\lambda_{FR}$. This reduction of $\Delta\lambda_{FR}$ is marked by the tapering region indicated by the red dotted lines in the figure. Also, the spectral width of the FR due to DM and CM becomes sharper and narrower with increased intensity and reduced CCS, consequently approaching the typical asymmetric FR nature. In Fig. 3(f), the degree of asymmetry of FRD_{DM} gets so much modulated that the FRD_{DM} appears like a narrow induced reflectance dip (IRD) in the center of a broad reflectance peak.

Now if we compare Figs. 2(b) and 3(b), we observe a spectral flipping of FRD_{CM} and FRD_{DM} for the same CCS value (290 nm) but different pump intensities. Such a flipping can be attributed to mirror image formation due to CCP alteration resulting from different pairs of intensity, leading to varying refractive index, for a fixed CCS value. This is in agreement with the same explanation for the occurrence of mirror image formation of FR dips for different pairs of CCS for a particular refractive index.[9]

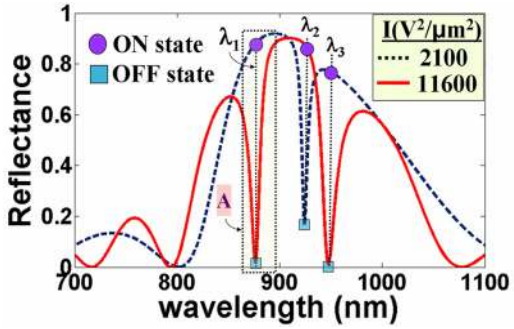

FIG. 7. Reflectance spectrum for two different input intensities revealing optical switching, and the switching wavelengths are marked by λ_1, λ_2, and λ_3, where $\lambda_1 = 876.3$ nm, $\lambda_2 = 924.1$ nm, and $\lambda_3 = 947.5$ nm. Here CCS = 400 nm. The ON and OFF states are depicted by filled circles and squares, respectively.

B. Evolution of IRD and DIRD

When one of the FR modes become distinct and markedly sharper and narrower than the other(s), it transpires itself in the form of an emerging resonance in the center of a broad spectral response. In our case, it appears as IRD in the center of a broad reflectance peak as can be observed from Fig. 4. On enhancing the intensity from 1000 $V^2/\mu m^2$ [in Fig. 4(a)] to 6300 $V^2/\mu m^2$ [in Fig. 4(b)], an IRD originates, seeming to arise from the bifurcation of the reflectance peak of Fig. 4(a). In the consequent figures [Figs. 4(c) and 4(d)], the reflectance value lowers (i.e., the IRD deepens) on successive increment of intensity. With further application of higher intensities, both the FR dips start becoming prominent and appear as DIRD as observed from Figs. 4(e) and 4(f). The spectral distance between the two dips of DIRD is defined as $\Delta\lambda_{DIRD}$ as indicated in the figure. As IRD (analogously PIT) is a class of FR, DIRD can also be considered as dual (or double) PIT, thus reflecting DFR.

The existence of DIRD for different intensity values is depicted in Fig. 5 for another value of CCS = 315 nm. On close investigation of plots (a) to (f) in Fig. 5(i), it is observed that the two resonant dips of DIRD become closer

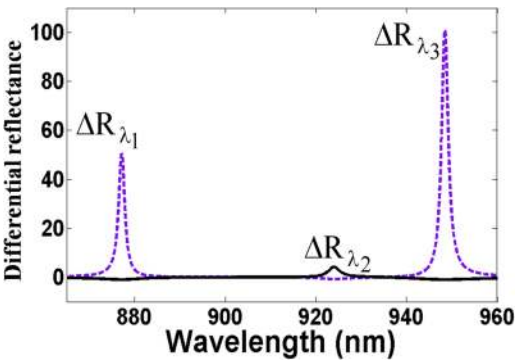

FIG. 8. Differential reflectance (ΔR) versus wavelength plot for triple wavelength switching.

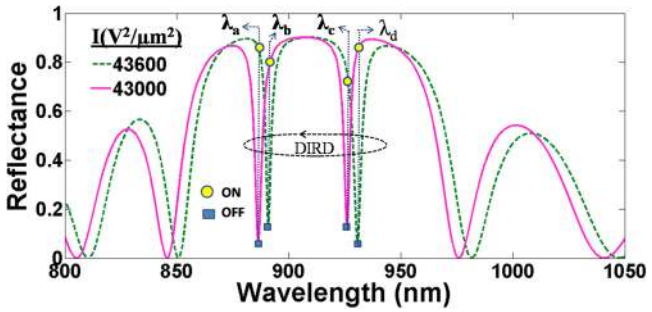

FIG. 9. Two DIRD plots for four wavelength switching (CCS = 400 nm). The four SWs are $\lambda_a = 886.3$ nm, $\lambda_b = 890.8$ nm, $\lambda_c = 926$ nm, and $\lambda_d = 930.6$ nm.

and narrower with a gradual increase in intensity. This inference is quantitatively confirmed through graphical analysis in Fig. 5(ii) which depicts the behavior of $\Delta\lambda_{DIRD}$ as a function of pump intensity. The plot ensures reduction of $\Delta\lambda_{DIRD}$ with increasing applied intensity for a fixed value of CCS.

C. Multiple Fano resonance

From the contour plot of Fig. 6, which depicts the reflectance profile for varying intensity and wavelength, it is observed that for a fixed wavelength band, the number of Fano modes increases with increasing intensity. For a detailed explanation, the wavelength band denoting the occurrence of Fano dips due to discrete mode and continuum mode is marked by bands ABCD and PQRS, respectively. In each of these, for a lower intensity region, marked by boxes 1 and 3, very few modes are observed compared to the large number of modes marked by boxes 2 and 4 in the higher intensity regime. The blue dots denoting lower intensity indicates the reflectance dips in the figure. The multiple dips account for the MIRD leading to the occurrence of MFR. Application of MFR to implement multispectral switching is explored in Sec. IV.

IV. APPLICATION IN OPTICAL SWITCHING

A. Single wavelength optical switching and introduction to multispectral switching (MS)

Modulation of the permittivity of the Kerr medium by controlling the pump beam intensity results in the shift of spectral characteristics, and this feature is utilized to achieve optical switching in the plasmonic system. Since in our investigations the reflected signal is treated as the output beam, high and low reflectance denote ON and OFF state, respectively. Ideally, 0% and 100% reflectance shall mean an OFF and ON state, respectively, but practically in the results obtained, OFF and ON states are considered below and above a threshold reflectivity value of 0.2 and 0.5, respectively.

Figure 7 depicts optical switching using the spectral response for two pump intensities. To begin with, let us demonstrate optical switching at a single wavelength (λ_1) for which we consider block "A" highlighting high reflectance at $\lambda_1 = 876.3$ nm for $I = 2100\ V^2/\mu m^2$ and very low reflectance for $I = 11\,600\ V^2/\mu m^2$ at the same wavelength. Thus, by switching the intensity from one value to another, the signal is made to transit from a high value (ON-state) to a low value (OFF-state) or vice versa at a particular wavelength known as the switching wavelength (SW). This enables the device to switch between ON and OFF states at the SW and hence serving as an optical switch. The same mechanism is valid for optical switching at $\lambda_2 = 924.1$ nm and $\lambda_3 = 947.5$ nm. Since in this case, switching operation is achieved simultaneously at three wavelengths (λ_1, λ_2, λ_3), the device can now be utilized as a multispectral switch. In Fig. 7, out of λ_1, λ_2, and λ_3, any two SWs can be used for dual wavelength switching as well. Moreover, the DFR dips are seen to provide the switching at λ_1 and λ_3.

The efficiency of the optical switch can be quantitatively determined through the evaluation of differential reflectance,

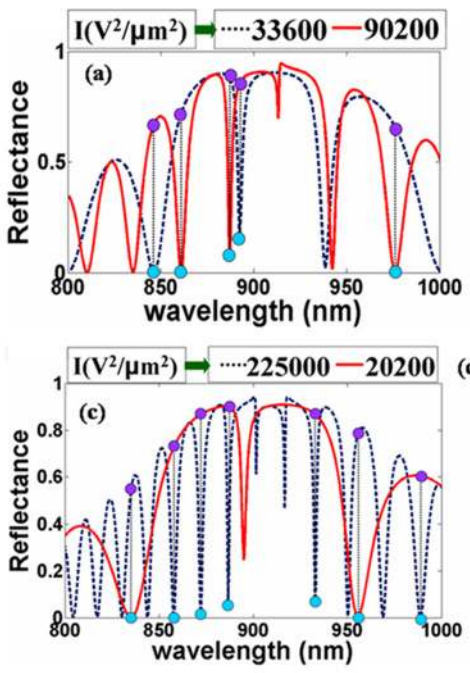

Number of switching wavelengths (from blue towards red spectrum)	Switching Wavelengths (nm)		
	Five wavelength switching	Six wavelength switching	Seven wavelength switching
1st	846.5	849.3	835.0
2nd	861.0	865.6	857.8
3rd	887.0	882.3	872.2
4th	892.5	890.2	886.7
5th	976.0	935.3	895.0
6th	-	964.3	933.0
7th	-	-	955.5

FIG. 10. Optical switching at (a) five, (b) six, (c) seven wavelengths (CCS = 400 nm), and the corresponding SWs shown in (d).

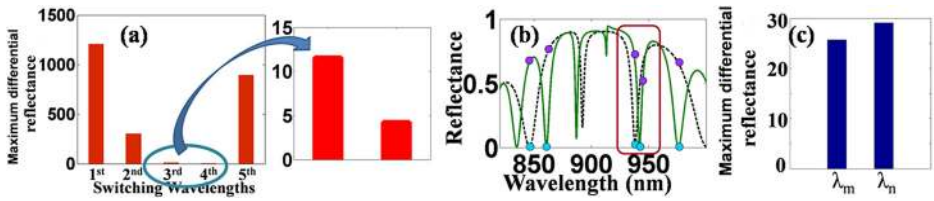

FIG. 11. (a) ΔR_{max} plot at the five switching wavelengths with a zoomed image for the 3rd and 4th switching wavelengths depicted alongside. (b) shows the modified five wavelength switching, and (c) depicts ΔR_{max} for the new 3rd and 4th switching wavelengths.

$\Delta R = (R_{ON} - R_{OFF})/R_{OFF}$, where R_{ON} and R_{OFF} denote the reflectance at ON and OFF states, respectively. ΔR is obviously seen to obtain high values at the SWs as illustrated in Fig. 8 which is plotted corresponding to the optical switching depicted in Fig. 7. The maximum differential reflectance given by ΔR_{max} is calculated from the graph of Fig. 8 and is evaluated to be 50.4, 4.2, and 101 at λ_1, λ_2, and λ_3, respectively. Higher ΔR_{max} reveals higher switching efficiency (SE). High SE at $\lambda_1$and λ_3 compared to that of λ_2 has resulted from very low reflectance value at these two wavelengths. Moreover, SE is almost double in case of switching at λ_3 compared to that of λ_1. This is because of almost a twofold reduction of the reflectance value at λ_3 with respect to λ_2 during their corresponding OFF states as calculated from the corresponding plots.

B. Implementation of DIRD in four wavelength switching

The spectral shift of DIRD with modulation of input intensity producing resonant dips at four wavelengths λ_a, λ_b, λ_c, and λ_d is illustrated in Fig. 9. The switching principle is the same as that of the previous cases. ΔR_{max} manifesting the switching efficiency at λ_a, λ_b, λ_c, and λ_d is evaluated to be 12.48, 5.02, 5.04, and 12.13, respectively.

C. Implementation of MIRD for multispectral switching at higher number of wavelengths

The optical switching at 5, 6, and 7 wavelengths can also be achieved with modulation of the applied intensity as shown in Figs. 10(a)–10(c), respectively, and the numerical value of the SWs is tabulated in Fig. 10(d). This multispectral switching beyond four wavelengths can be attributed to MIRD arising from MFR.

ΔR_{max} analysis can be effectively used to choose efficient optical switching. As an example, let us initially evaluate ΔR_{max} for switching at five wavelengths [Fig. 10(a)]. ΔR_{max} presented as bar plots in Fig. 11(a) is seen to yield ultra high values of 1208, 303, and 895 (rounded off values) at the 1st, 2nd, and 5th SWs. On the other hand, very low values of $\Delta R_{max} = 11.62$ and 4.3 are obtained for switching at the 3rd and 4th wavelength, respectively [as is clear from the zoomed section of Fig. 11(a)]. This is due to the fact that the value of the reflectance dip at these wavelengths are not negligible compared to the almost zero reflectance dips at 1st, 2nd, and 5th switching wavelengths. Now if we choose two new wavelengths $\lambda_m = 938$ nm and $\lambda_n = 942$ nm [from Fig. 10(a)] in place of the original 3rd and 4th SW, it provides $\Delta R_{max} = 26$ and 29 (rounded off) which is almost two and sevenfold higher than that achieved at the original SWs. Thus, we now substitute the 3rd and 4th SWs at 938 nm and 942 nm instead of 887 and 892.5 nm. Thus, by evaluating ΔR_{max} one can choose the switching wavelengths yielding higher switching efficiency manifested in terms of maximum differential reflectance. The modified five wavelength switching is illustrated in Fig. 11(b) and the corresponding bar plot showing ΔR_{max} considering the new SWs is demonstrated in Fig. 11(c). ΔR_{max} for six and seven wavelength switching as calculated from Figs. 10(b) and 10(c) is plotted in Fig. 12.

V. Q-FACTOR TUNING AT FIXED WAVELENGTH BY SPECIFIC INTENSITY MODULATION

Modulation of the pump beam intensity usually brings about a shift in the resonant wavelengths, and such a shift is generally utilized to cause the device to operate as an on-off switch. But, however, unlike that of the switching phenomenon, it has been found that for certain chosen specific intensity values of the pump excitation, one of the resonant dips in the spectrum merges at a fixed wavelength for all curves corresponding to different intensities, and the spectral width of the coincident resonant dips is different for each curve. This is clarified from Fig. 13. Figure 13(a) shows the reflected spectra for four different intensities. For these certain specific intensities, one of the dips of all the curves is seen to merge at 928.5 nm, and the spectral bandwidth is observed to be different for each intensity value. For better clarity, the zoomed portion of the reflectance dips at 928.5 nm is depicted in Fig. 13(b) which reveals that the spectral width becomes narrower with an increase in applied intensity. To confirm the phenomenon, another set of reflected

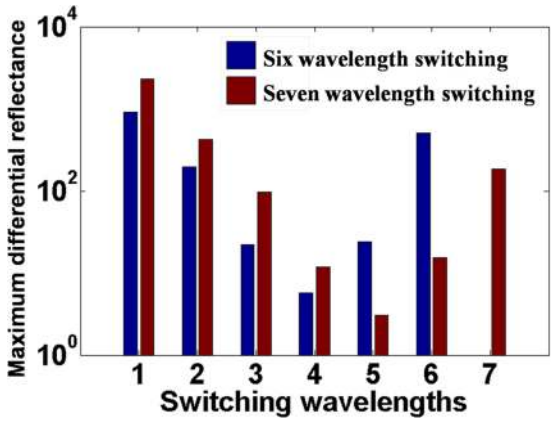

FIG. 12. Maximum differential reflectance plot (in log scale) for six and seven wavelength switching.

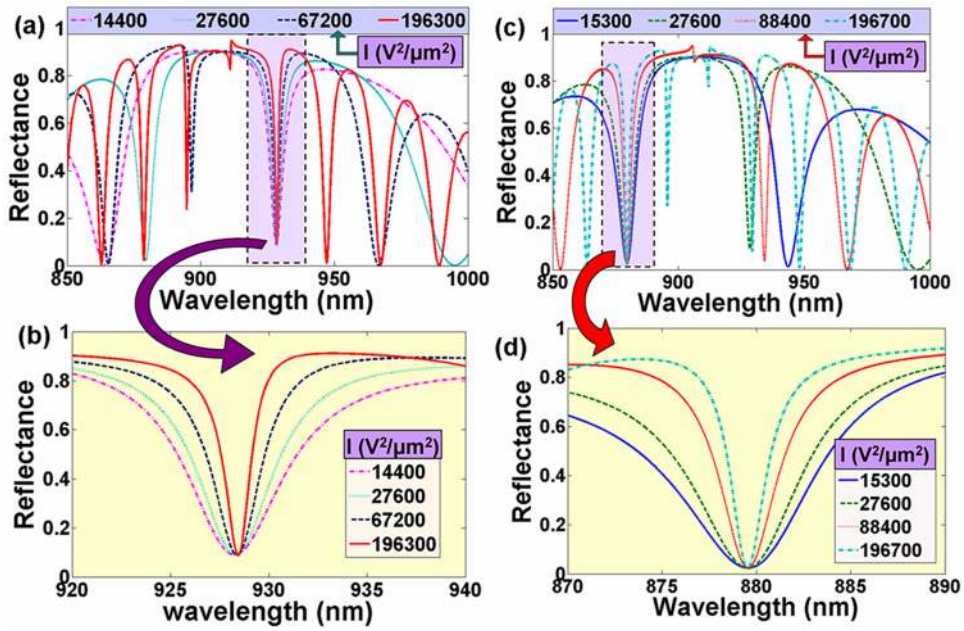

FIG. 13. Spectral width tuning (CCS = 400 nm) at a fixed wavelength of (a and b) 928.5 nm and (c and d) 879.5 nm.

spectra is shown in Fig. 13(c) which ensures the merging of one of the resonance dips at a particular wavelength of 879.5 nm, for all the four spectra corresponding to different specific intensities. Spectral width reduction with enhanced intensities is also evident from Fig. 13(d). Thus, spectral width manipulation manifesting bandwidth tuning is depicted for two fixed central wavelengths of 928.5 nm and 879.5 nm, by launching the pump beam at specific intensities with narrower spectrum achieved at higher intensity values in each case. Tuning the bandwidth in this manner provides a platform for the device to be used as a tunable band-stop filter with the advantage of requiring only an external beam intensity modulation compared to the structural alteration requirement to achieve band-pass or band-stop filtering in other plasmonic waveguide coupled devices.[11,12] Moreover, such a filter application is much desired where bandwidth tuning is required without changing the operating frequency.

Quantitative evaluation of the spectral width tuning is performed by determining the Quality factor (Q-factor) which provides a Figure of Merit for analysis of cavity based systems and is mathematically defined as[41,42]

$$\mathrm{Q-factor} = \frac{\lambda_O}{\mathrm{FWHM}}, \tag{5}$$

TABLE I. Quality factor calculation for two fixed operating wavelengths.

Wavelength (nm)	Specific intensity values ($V^2/\mu m^2$)	FWHM (nm)	Quality factor
928.5	1 440	6.2	179.76
	27 600	4.7	197.55
	67 200	3.0	309.50
	196 300	1.6	580.31
879.5	15 300	10.7	82.20
	27 600	7.8	112.76
	88 400	4.0	219.87
	196 700	2.4	366.46

where FWHM denotes the full width half maxima of the spectrum and λ_O is the operating or resonant wavelength. The FWHM and the corresponding Q-factor of the merged resonant profiles are calculated from Fig. 13 for two operating wavelengths and are tabulated in Table I. For both the operating wavelengths, it is observed that FWHM reduces with an increment of intensity and evidently the Q-factor is higher for higher applied intensity. The highest Q-factor corresponding to the highest intensity ensures higher energy confinement for narrower spectrum. Moreover, quantitative evaluation suggests that an extremely low FWHM of 1.6 nm can be obtained revealing the achievement of ultra narrow line shapes with an appreciably good Quality factor. Also, the maximum calculated FWHM is only 10.7 nm, and thus we can infer that fine filtering can be achieved using this device. Very low FWHM exhibiting ultra narrow FR line shape is accounted to nonlinearity effect and the presence of dual cavities enabling higher coupling efficiency.

VI. CONCLUSION

Dual and multiple Fano resonance have been investigated through the incorporation of a third order Kerr nonlinear medium in a nanoplasmonic waveguide coupled cavity system. The increment of pump beam intensity along with the reduction of cavity-cavity separation of the structure leads to narrower FR line shapes and reduced spectral separation between the FR dips. Spectral flipping of $\mathrm{FRD_{DM}}$ and $\mathrm{FRD_{CM}}$ is also obtained via CCP control through intensity modulation. Generation of DIRD from IRD and subsequent evolution of MIRD with a suitable and gradual increment of intensity is exhibited. Spectral shift of FR dips due to alteration of nonlinear permittivity is applied to achieve optical switching, and DIRD and MIRD are utilized to implement the device as a multispectral nanoplasmonic switch. Multispectral switching up to seven wavelengths is demonstrated along with switching efficiency evaluation in terms of maximum differential reflectance. Such a performance

evaluation is utilized to enhance the efficiency of the switch at certain switching wavelengths. Apart from this, bandwidth tuning of multiple resonances at a particular wavelength is demonstrated for two center frequencies and both cases ensure the achievement of ultra narrow FWHM along with the enhancement of the quality factor with increased intensity of the pump excitation. Such spectral width tuning is advantageous where tunable filtering is required without changing the operating frequency which can be achieved simply by controlling the external pump excitation without the need for any structural modification.

ACKNOWLEDGMENTS

The author S. Paul acknowledges the Department of Science and Technology (DST), Govt. of India, for providing Senior Research Fellowship (SRF) under the INSPIRE fellowship scheme.

[1]W. L. Barnes, A. Dereux, and T. W. Ebbesen, Nature **424**, 824 (2003).
[2]M. J. Zhang, L. Zhang, and W. Xu, J. Phys. D Appl. Phys. **45**, 113001 (2012).
[3]Y. Huang, C. Min, L. Yang, and G. Veronis, Int. J. Opt. **2012**, 372048 (2012).
[4]Y. Xiang, X. Zhang, W. Cai, L. Wang, C. Ying, and J. Xu, AIP Adv. **3**, 012106 (2013).
[5]P. Neutens, P. V. Dorpe, I. D. Vlamink, L. Lagae, and G. Borghs, Nat. Photonics **3**, 283 (2009).
[6]Y. Xiang, W. Luo, W. Cai, C. F. Ying, X. Yu, X. Zhang, H. Liu, and J. Xu, Opt. Express **24**, 3849 (2016).
[7]S. Paul and M. Ray, Appl. Phys. A **122**, 21 (2016).
[8]A. E. Miroshnichenko, S. Flach, and Y. Kivshar, Rev. Mod. Phys. **82**, 2257 (2010).
[9]S. Paul, M. Bera, and M. Ray, J. Lightwave Technol. **33**, 2824 (2015).
[10]S. Zhan, Y. Peng, Z. He, B. Li, Z. Chen, H. Xu, and H. Li, Sci. Rep. **6**, 22428 (2016).
[11]M. F. Limonov, M. V. Rybin, A. N. Poddubny, and Y. S. Kivshar, Nat. Photonics **11**, 543 (2017).
[12]S. Hayashi, D. V. Nesterenko, and Z. Sekkat, Appl. Phys. Express **8**, 022201 (2015).
[13]K. J. Boller, A. Imamolu, and S. E. Harris, Phys. Rev. Lett. **66**, 2593 (1991).
[14]X. Piao, S. Yu, and N. Park, Opt. Express **20**, 18994 (2012).
[15]H. Lu, X. Liu, G. Wang, and D. Mao, Nanotechnology **23**, 44403 (2012).
[16]S. Paul and M. Ray, IEEE Photon. Technol. Lett. **29**, 739 (2017).
[17]H. Lu, X. Liu, D. Mao, Y. Gong, and G. Wang, Opt. Lett. **36**, 3233 (2011).
[18]Y. Xiao, M. Li, Y. Liu, Y. Li, X. Sun, and Q. Gong, Phys. Rev. A **82**, 065804 (2010).
[19]B. Wang, Q. Zeng, S. Xiao, C. Xu, L. Xiong, H. Lv, J. Du, and H. Yu, J. Phys. D Appl. Phys. **50**, 455107 (2017).
[20]S. X. Xia, X. Zhai, Y. Huang, J. Q. Liu, L. L. Wang, and S. C. Wen, J. Lightwave Technol. **35**, 4553 (2017).
[21]S. X. Xia, X. Zhai, L. L. Wang, and S. C. Wen, Photonics Res. **6**, 692 (2018).
[22]S. X. Xia, X. Zhai, L. L. Wang, B. Sun, J. Q. Liu, and S. C. Wen, Opt. Express **24**, 17886 (2016).
[23]B. Dana and A. Bahabad, Opt. Express **24**, 22334 (2014).
[24]D. Wang, X. Yu, and Q. Yu, Appl. Phys. Lett. **103**, 053117 (2013).
[25]J. Qi, Z. Chen, J. Chen, Y. Li, W. Qiang, J. Xu, and Q. Sun, Opt. Express **22**, 14688 (2014).
[26]Z. Chen, X. Song, G. Duan, L. Wang, and L. Yu, IEEE J. Photonics **7**, 2701009 (2015).
[27]J. Yang, X. Song, S. Yang, L. Cui, and L. Yu, J. Phys. D Appl. Phys. **50**, 325107 (2017).
[28]A. Pannipittiya, I. D. Rukhlenko, and M. Premaratne, J. Opt. Soc. Am. B **28**, 2820 (2011).
[29]M. Kauranen and A. V. Zayats, Nat. Photonics **6**, 737 (2012).
[30]S. Paul and M. Ray, J. Appl. Phys. **120**, 203102 (2016).
[31]Z. He, H. Li, S. Zhan, B. Li, Z. Chen, and H. Xu, Sci. Rep. **5**, 15837 (2015).
[32]H. Lu, X. Liu, L. Wang, Y. Gong, and D. Mao, Opt. Express **19**, 2910 (2011).
[33]X. Lin, J. Yan, Y. Zheng, L. Wu, and S. Lan, Opt. Express **19**, 9594 (2011).
[34]X. Kang, H. Li, and L. Wen, Optik **134**, 21 (2017).
[35]L. Stern, M. Grajower, and U. Levy, Nat. Commun. **5**, 4865 (2014).
[36]J. Homola, Sens. Actuators **41**, 207 (1977).
[37]S. Collin, F. Pardo, and J. L. Pelouard, Opt. Express **15**, 4310 (2007).
[38]S. Fan, W. Suh, and J. D. Joannopoulos, J. Opt. Soc. Am. A **20**, 569 (2003).
[39]H. Lu, X. Liu, D. Mao, and G. Wang, Opt. Lett. **37**, 3780 (2012).
[40]X. Wang, H. Jiang, J. Chen, P. Wang, Y. Lu, and H. Ming, Opt. Express **19**, 19415 (2011).
[41]S. Paul and M. Ray, J. Opt. **42**, 203 (2013).
[42]S. Paul and M. Ray, Advances in Optical Science and Engineering (Springer Nature, Singapore, 2017), Vol. 194, Chap. 66, pp. 529–534.